Contents lists available at ScienceDirect

Transactions of Nonferrous Metals Society of China

36(2026) 552−570

www.tnmsc.cn

Multiscale investigation of oxidation mechanism in AlCrSiN multilayer coatings via experiments and ab initio molecular dynamics

Ji-yuan LIU [a,b], Shu-bing HU [a,b*], Bo PENG [a,b], Jing-jing TIAN [a,b], Si-qi ZENG [c], Hai-xin CHANG [a,b], Hong-ya LI [a,b], Jin-ke YU [a,b], Fei GUO [d,e]

[a] State Key Laboratory of Material Processing and Die & Mould Technology, Huazhong University of Science and Technology, Wuhan 430074, China;

[b] School of Materials Science and Engineering, Huazhong University of Science and Technology, Wuhan 430074, China;

[c] Institute of Applied Physics, Jiangxi Academy of Sciences, Nanchang 330096, China;

[d] School of Electronic Engineering, Guangxi University of Science and Technology, Liuzhou 545006, China;

[e] Liuzhou Key Laboratory of New Energy Vehicle Power Lithium Battery, Guangxi University of Science and Technology, Liuzhou 545006, China

Abstract: An advanced AlCrSiN/AlCrN/CrN/Cr multilayer coating was developed via hybrid multiarc ion plating and high-power impulse magnetron sputtering. The multilayer design enhanced the substrate–coating compatibility, achieving a critical load of 87.8 N. Silicon doping induced nanocrystallization and amorphization, increasing the hardness to 26 GPa. At high temperatures, a nanoscale Cr-rich $(Cr,Al)_2O_3$ layer was formed, effectively inhibiting oxygen diffusion. The coating underwent unique phase transformations, during which Cr_2N and amorphous Si_3N_4 were converted into dispersed $SiCr_3$ nanoparticles, which stabilized Cr atoms and suppressed their outward diffusion. Ab initio molecular dynamics simulations revealed that Cr atoms exhibited higher chemical activity and oxygen-capture capability than Al atoms and Si atoms served as diffusion barriers by pinning onto the oxidized surface, considerably improving the oxidation resistance of the coating.

Keywords: physical vapor deposition; AlCrSiN coating; oxidation; AIMD simulation

1 Introduction

Mold-forming technology plays a pivotal role in modern industrial manufacturing, particularly in hot forging and stamping processes, during which molds are subjected to extreme thermomechanical stresses. Under these conditions, molds are subjected to severe impact loading [1], abrasive wear [2], and thermal fatigue failure [3], necessitating advanced surface protection strategies. Physical vapor deposition has emerged as a transformative surface engineering approach [4,5], and AlCrN coatings are being widely adopted because of their exceptional hardness [6,7], high oxidation resistance [6,8], and excellent tribological properties [7,9]. However, the application of conventional AlCrN coatings on emerging advanced difficult-to-form materials remains limited, prompting the development of enhanced protective solutions [10−12].

Recent studies have demonstrated that Si doping with AlCrN coatings induces a unique nanocomposite structure in which amorphous Si_3N_4 phases are interwoven with nanocrystalline (Al,Cr)N networks [13,14]. The optimal incorporation of Si (3−5 at.%) considerably enhances the coating performance, achieving simultaneous improvements in hardness [15], wear resistance [16], and oxidation

Corresponding author: *Shu-bing HU, Tel: +86-13995667466, E-mail: hushubing@hust.edu.cn

https://doi.org/10.1016/S1003-6326(25)66981-0

Received 3 September 2024; accepted 23 May 2025

resistance [17] while maintaining adequate fracture toughness [15,18,19]. The performance enhancement results from the synergistic nanocrystalline-strengthening and amorphous-phase reinforcement mechanisms.

Despite these advancements, coating–substrate adhesion remains a critical challenge. Although Si doping increases the coating hardness [15,17], it may intensify interfacial stresses owing to the disparity between the physicochemical properties, potentially causing premature spalling [20]. Multilayer architectures featuring gradient transition designs can effectively address the aforementioned issues [2,10,17]. Such designs enhance interfacial compatibility via controlled gradients in the chemical composition, stress distribution, mechanical properties, and thermal expansion coefficients [21,22]. Furthermore, multiple interfaces in these coatings serve as barriers to crack propagation [23,24]. CAI et al [15] demonstrated that AlCrSiN coatings with Si content gradients exhibited higher hardness and lower elastic modulus than their single-layer counterparts. This gradient design mitigates the "eggshell effect" at the coating–substrate interface, thereby improving adhesion. Additionally, the gradient coatings exhibit superior tribological performance and extended tool life compared to homogeneous coatings.

Oxidation resistance is a critical performance metric for hot-work mold coatings, in which Si doping results in particular benefits. POLCAR and CAVALEIRO [25] confirmed that AlCrSiN maintained thermal stability up to 1300 °C. JÄGER et al [18] systematically investigated the effects of Si content on AlCrSiN oxidation behavior, observing that the oxidation onset temperature increased from 1100 to 1260 °C with increasing Si content. At high temperatures, in situ-formed $SiCr_3$ nanoparticles inhibit the outward diffusion of Cr, facilitating the formation of a protective Al_2O_3-rich surface layer that considerably enhances the oxidation resistance.

Although experimental studies have provided valuable insights into the oxidation behavior of coatings, the atomic-scale mechanisms remain unclear [26]. The development of density functional theory and ab initio molecular dynamics (AIMD) simulations has revolutionized the study of surface oxidation processes [27]. For instance, XIE et al [8] employed AIMD to investigate CrAlN oxidation at 1123 K, revealing considerable electron transfer from Cr to O atoms that formed a dense (Cr,Al)-oxide surface layer, inhibiting further oxidation. GUO et al [28] modeled TiAlN coatings doped with V, Hf, and Si atoms, demonstrating that Si and Hf doping improved the high-temperature oxidation resistance, whereas V doping exerted negligible effects. However, AIMD studies on Si-doped CrAlN coatings remain scarce.

This study pioneers the investigation of the dynamic coupling between phase transformation and protective oxide-layer formation in Si-doped AlCrN multilayer coatings under high-temperature conditions via integrated experimental characterization and AIMD simulations. Using a hybrid deposition system combining multiarc ion sources (ARC) and high-power impulse magnetron sputtering (HiPIMS), AlCrN/AlCrSiN multilayer coatings were successfully fabricated on 3Cr2W8V hot-work die steel substrates. We systematically evaluated the effects of the transition layer architecture and Si doping on the microstructure evolution, adhesion properties (achieving critical loads up to 87.8 N), mechanical performance, and oxidation resistance. Complementary AIMD calculations were performed to elucidate the atomic-scale structure–activity relationship between the electronic structure and oxidation resistance. This multiscale approach provides comprehensive insights from macroscopic to atomic levels, offering practical guidelines for the design of next-generation protective coatings for exigent industrial applications.

2 Experimental and computation

2.1 Coating deposition

In this study, heat-treated 3Cr2W8V mold steel substrates (20 mm × 20 mm × 5 mm) were used for coating deposition. Multilayer AlCrSiN/AlCrN/CrN/Cr (designated as multi-AlCrSiN) coatings (Fig. S1 in Supporting Information (SI)) were deposited using the HCMS-CA-650 vacuum coating system (Fig. S2 in SI), which was jointly developed by Huazhong University of Science and Technology and Guangdong Huicheng Vacuum Technology Co., Ltd. The system features two ARC, two HiPIMS sources, and an arc electron generator (AEG). The AEG generates an exceptionally high plasma density in an Ar/N_2 atmosphere through arc discharge, enabling more efficient glow-ion nitriding with superior results compared with conventional processes.

Before deposition, the substrates were subjected to AEG-assisted ion nitriding to enhance their surface hardness (Fig. S3 in SI). The deposition sequence began with the deposition of a Cr/CrN base layer via ARC using a pure Cr target. Subsequently, AlCrSiN and AlCrN top layers were deposited using HiPIMS, employing AlCrSi (Al∶Cr∶Si=6∶3∶1, molar ratio) and AlCr (Al∶Cr=7∶3, molar ratio) targets, respectively. The HiPIMS technique was used to minimize metal droplet formation and improve the coating surface quality.

Sample preparation included mechanical polishing followed by ultrasonic cleaning in ethanol and acetone. Detailed deposition parameters for each layer are given in Table 1. For a comparative analysis of the multilayer effects, the AlCrN/CrN/Cr (designated as single-AlCrN; Fig. S4 in SI) and AlCrSiN/CrN/Cr (designated as single-AlCrSiN; Fig. S5 in SI) coatings were prepared using identical processes.

Table 1 Deposition process of AlCrSiN coating

Deposition step	Deposition process
AEG ion cleaning	Ar flow rate 750 cm^3/min, sample bias −800 V, AEG power 2.8 kW, and deposition time 30 min
AEG ion nitriding	N_2 flow rate 750 cm^3/min, Ar flow rate 100 cm^3/min, AEG power 2.8 kW, sample bias −600 V, and deposition time 120 min
Metal Cr deposition	Ar flow rate 200 cm^3/min, Cr target power 2.4 kW, duty cycle 50%, sample bias −100 V, and deposition time 90 min
CrN layer deposition	Ar flow rate 100 cm^3/min, N_2 flow rate 500 cm^3/min, Cr target power 2.4 kW, duty cycle 50%, sample bias −100 V, and deposition time 90 min
AlCrN layer deposition	Ar flow rate 220 cm^3/min, N_2 flow rate 55 cm^3/min, AlCr target power 2.8 kW, duty cycle 8%, sample bias −100 V, and deposition time 150 min
AlCrSiN layer deposition	Ar flow rate 220 cm^3/min, N_2 flow rate 55 cm^3/min, AlCr target power 2.8 kW, duty cycle 8%, sample bias −100 V, and deposition time 300 min

2.2 Mechanical and adhesion performance testing

The mechanical properties of the coatings were systematically characterized using a Bruker TI750 nanoindenter to measure the hardness and elastic modulus. Each sample was subjected to five tests at a maximum load of 6 mN after surface polishing to eliminate contamination effects. Adhesion properties were evaluated using an Anton Paar RST scratch tester through 5 mm scratch tests under progressively increasing loads up to 100 N, and the critical loads L_{c1} (indicating first cohesive cracking within the track) and L_{c2} (representing initial adhesive spallation at scratch edges) were determined through subsequent optical microscopy examination of the scratch morphology.

2.3 Oxidation experiments

The high-temperature oxidation resistance of the coatings was evaluated via two complementary experimental approaches. First, the samples were oxidized in a muffle furnace at 850 °C for 8 h in ambient atmosphere. The thickness of the oxide layer was then measured using SEM to quantify the oxidation resistance. For an in-depth thermal analysis, multi-AlCrSiN coatings were deposited on Al_2O_3 substrates (5 mm × 5 mm × 1 mm) and characterized using a Netzsch STA 449F5 simultaneous thermal analyzer (TGA−DSC). Comparative oxidation tests were conducted using a thermal analyzer in air and argon atmospheres at a controlled heating rate of 10 °C/min from room temperature (25 °C) to 1000 °C, followed by a 1 h isothermal holding to assess the coating stability under prolonged thermal exposure.

2.4 Structural characterization

The structural and compositional characteristics of the coatings were comprehensively examined using multiple advanced analytical techniques. Phase analysis was performed using grazing-incidence X-ray diffractometry (GIXRD, Shimadzu XRD−6100) utilizing Cu K_α radiation at a fixed incident angle of 1° in the scanning range of 20°−90° at 2 (°)/min with continuous stage rotation to minimize orientation effects. Microstructural examination was conducted using a field-emission SEM instrument (FEI Nova NanoSEM 450) operated at 20 kV, coupled with an energy-dispersive X-ray spectroscopy (EDS) system (Oxford X-Max 50) for semiquantitative compositional analysis. For nanoscale characterization using TEM, the samples were prepared via focused ion-beam milling (Thermo Fisher Helios 5) and subsequently analyzed using a field-emission TEM

instrument (FEI Tecnai G^2 F30) at 300 kV to investigate the internal microstructure and elemental distribution of the coatings. The surface chemical states were examined via XPS (Thermo Scientific K-Alpha), before the samples were subjected to Ar^+-ion sputtering to remove the surface contaminants.

2.5 Calculation methods

To elucidate the differences in the atomic-scale oxidation behavior of various coating structures, we conducted AIMD simulations on the AlN, $Cr_{0.5}Al_{0.5}N$, and $Cr_{0.5-X}Al_{0.5}Si_XN$ systems using the Vienna ab initio simulation package [29,30]. The simulations employed the projector-augmented wave method [31] to describe the ion–electron interactions and the Perdew–Burke–Ernzerhof generalized gradient approximation [32,33] for the electron exchange-correlation effects. The initial structures were constructed using a wurtzite-type hexagonal unit cell for AlN and NaCl-type cubic CrN (c-CrN) unit cells for the other systems, in which two symmetric Cr atoms were substituted with Al to create the desired compositions. Surface energy analyses confirmed minimal variation among different layer thicknesses (4-, 6-, and 8-layer models; Fig. S6 in SI), leading to the selection of computationally efficient 4-layer (100) surface-exposed 3 × 3 supercell containing 36 atoms per layer for the AIMD calculations.

The simulation setup featured fixed bottom two layers to represent the bulk material and relaxed top two layers to model the coating surface, employing a 15 Å vacuum layer and 9 O atoms positioned 3 Å above the surface (Fig. S7 in SI) to achieve 25% O coverage [34]. All the simulations used a timestep of 1 fs with an initial optimization of 2500 steps, a plane wave cutoff energy of 500 eV, and Γ-point-only Brillouin zone sampling [35]. The NVT ensemble was maintained at 1123 K using a Nosé–Hoover thermostat. The electronic convergence was set as 0.01 meV/atom, and a Gaussian smearing of 0.05 eV was applied for the Fermi-level integration. Spin polarization effects were not considered in these calculations.

3 Results and discussion

3.1 Morphology and structure

The surface morphologies of the as-deposited coatings are shown in Figs. 1(a–c). The single-AlCrN composite coating exhibits large-area shallow pits with sporadic microparticles while maintaining an

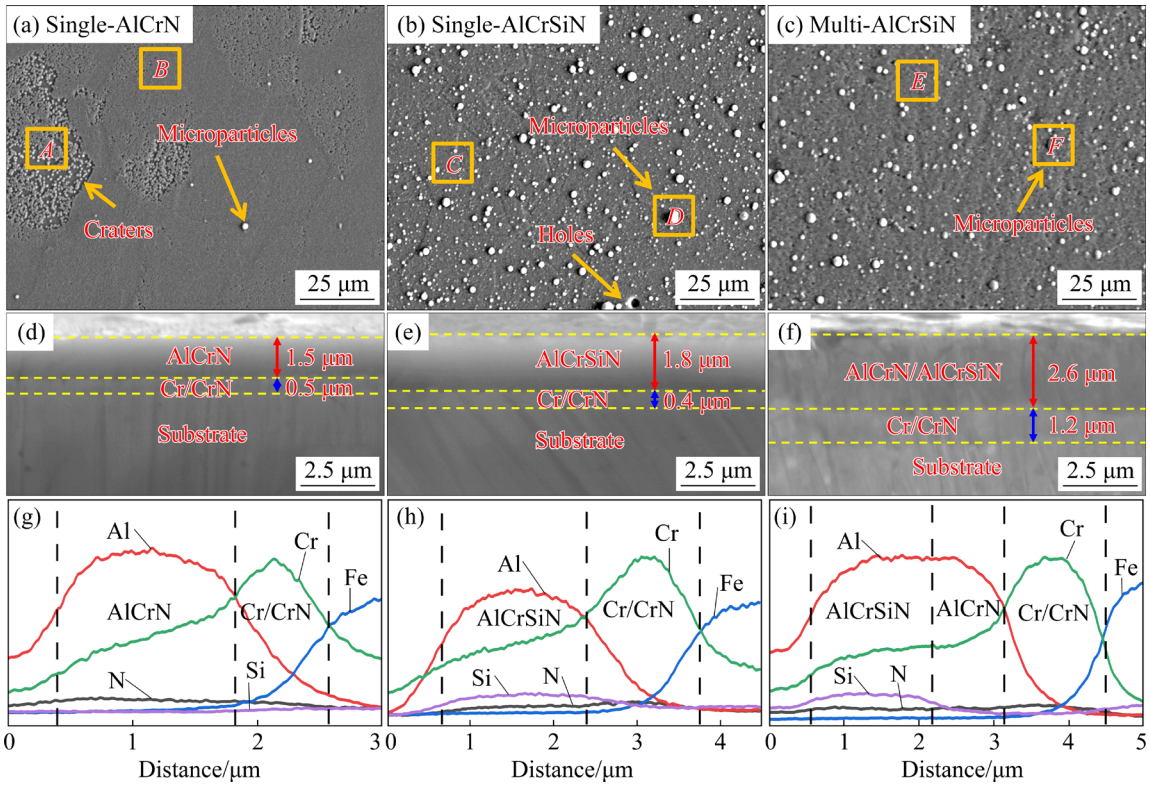

Fig. 1 SEM images (a−f) and corresponding EDS line scan results (g−i) of single-AlCrN (a, d, g), single-AlCrSiN (b, e, h), and multi-AlCrSiN (e, f, i) coatings: (a–c) Surface morphology; (d–f) Cross-sectional morphology

overall smooth and high-quality surface. The EDS analysis indicates similar elemental compositions in the pitted regions (Area *A*) and smooth areas (Area *B*), both featuring Cr, Al, and N elements, and the content of Al considerably exceeds that of Cr. Si incorporation through AlCrSi targets increases the microparticle formation during sputtering, which is evident on both the single-AlCrSiN and multi-AlCrSiN coating surfaces, which also feature minor deposition pores. The EDS results confirm that the microparticles comprise metal nitrides, demonstrating a substantially higher N content than that of the coating matrix. All coatings demonstrate complete substrate coverage without metal-droplet defects, exhibiting excellent surface quality. The N content in all the three coatings remains at <50% (Table 2) because of the formation of a Cr_2N phase during deposition. Although the Cr_2N phase may slightly compromise the coating's mechanical properties, the increased proportions of Al, Cr, and Si atoms within the coating composition contribute to the enhancement of the high-temperature performance of the coatings.

Table 2 Elemental compositions of as-deposited coatings in different regions in Fig. 1 (at.%)

Region	Cr	Al	Si	N	Fe
A	19.73	42.97	−	37.02	0.28
B	19.73	42.98	−	37.03	0.27
C	18.98	35.43	6.45	38.90	0.23
D	14.84	30.66	5.88	48.44	0.17
E	20.52	37.68	6.79	34.74	0.28
F	13.41	31.36	6.18	48.87	0.18

The cross-sectional structures and corresponding EDS line scan results of the three coatings are demonstrated in Figs. 1(d−f). The measured coating thicknesses are 2.0, 2.2, and 3.8 μm for single-AlCrN, single-AlCrSiN, and multi-AlCrSiN coatings, respectively, demonstrating a clear correlation between the thickness and process complexity. All the coatings display uniform equiaxed grain structures throughout their cross-sections. The layered architecture comprises a relatively thin Cr/CrN base layer dominated by Cr and a substantially thick Al-rich surface layer, in which the content of Al substantially exceeds that of Cr. In AlCrSiN-containing coatings, Si is uniformly distributed throughout the surface layer.

The multilayered design combines the excellent adhesion properties of the Cr-rich base layer with the superior high-temperature performance of the Al-rich surface layer. Furthermore, Si incorporation enhances the thermal stability of the coatings. The gradual transition in the composition between the layers minimizes the interfacial stress and improves the overall coating integrity.

Figure 2(a) shows the cross-sectional TEM bright-field image of the multi-AlCrSiN coating, which has a total thickness of 3.24 μm and three distinct compositional layers. The EDS mapping results in Figs. 2(e, f) reveal that the coating architecture comprises an inner Cr/CrN layer, intermediate AlCrN layer, and outer AlCrSiN layer, precisely corresponding to the deposition sequence. The AlCrN and AlCrSiN layers deposited via HiPIMS exhibit refined equiaxed grain structures, whereas the ARC-deposited Cr/CrN layer exhibits characteristic columnar growth and coarse grains.

The selected area electron diffraction (SAED) pattern of the AlCrSiN layer (Inset in Fig. 2(a)) shows diffraction rings corresponding to c-CrN and hexagonal AlN (h-AlN) phases together with an amorphous halo, confirming the presence of amorphous Si-containing phases. A thin CrN interlayer forms beneath the metallic Cr layer because of the residual N in the deposition chamber, and columnar Cr grains gradually transition to an equiaxed morphology in the CrN layer. SAED analysis reveals the predominant presence of the hexagonal Cr_2N (h-Cr_2N) phase in this region.

HRTEM images (Figs. 2(c, d)) reveal that the AlCrSiN layer features a nanocomposite structure composed of nanocrystalline domains embedded in an amorphous matrix, and the CrN layer displays grain boundaries aligned parallel to the growth direction. Fast Fourier transform (FFT) analysis demonstrates that these boundaries separate the h-Cr_2N and c-CrN phases.

3.2 Mechanical and adhesion properties

The mechanical and adhesion properties of coatings critically determine mold performance and service life. Figure 3(a) shows the hardness and elastic modulus of the three coatings. Notably, the hardness of coating increases with the structural complexity of the transition layers, and the multi-

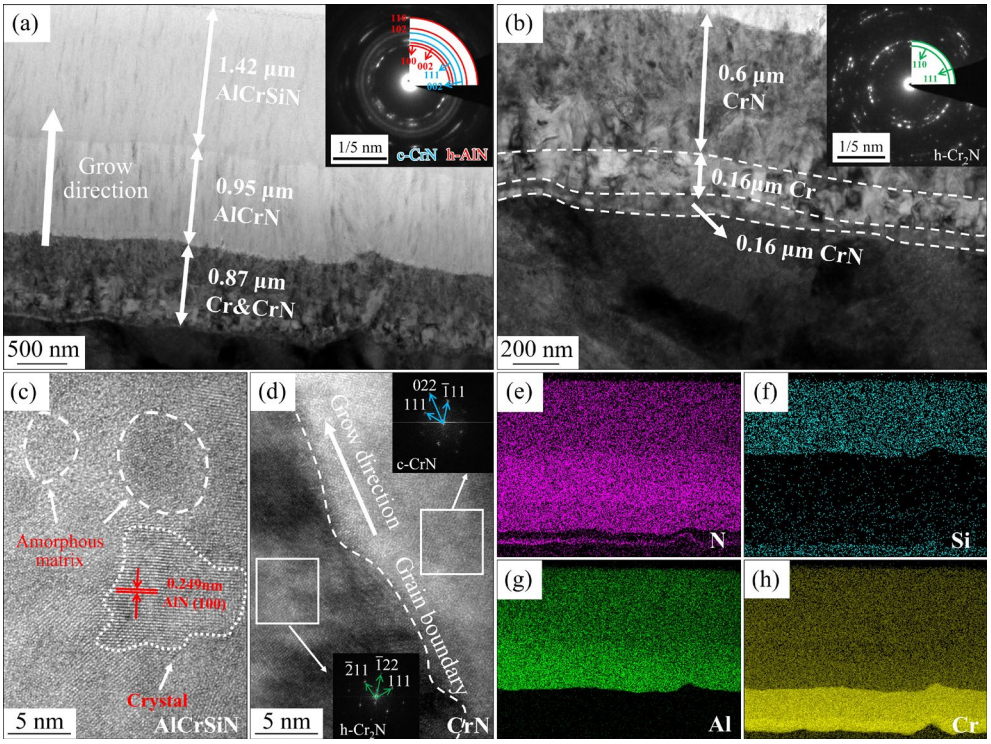

Fig. 2 (a, b) Bright-field images of deposited multi-AlCrSiN coating; (c, d) High-resolution TEM images of AlCrSiN and CrN layers, respectively; (e–h) EDS mapping of multi-AlCrSiN coating

AlCrSiN coating demonstrates the highest surface hardness of 26 GPa. However, the multi-AlCrSiN coating exhibits a considerably lower elastic modulus than the single-layer coating.

The hardness-to-elastic modulus ratio (H/E) serves as an effective indicator of the resistance of a coating to plastic deformation [36], and the H^3/E^2 ratio represents the coating toughness [37,38]. The enhanced toughness inhibits crack propagation during service, preventing coating delamination and extending the operational lifespan. As depicted in Fig. 3(b), the multi-AlCrSiN coating comprising the multilayer transition design demonstrates substantially higher toughness metrics than the single-AlCrN and single-AlCrSiN variants.

The load–displacement curves in Fig. 3(c) further support these findings. The elastic recovery ratio (W_e) was calculated using Eq. (1) [39], where h_{max} represents the maximum indentation depth, and h_f denotes the residual depth after unloading, providing additional quantification of toughness. The multi-AlCrSiN coating exhibited a W_e of 0.60, exhibiting superior toughness compared with the other tested samples. The proposed multilayer composite design effectively enhances the coating–substrate compatibility, facilitating the exceptional toughness while maintaining high surface hardness, which is a critical combination for demanding mold applications.

$$W_e = [(h_{max} - h_f)/h_{max}] \quad (1)$$

Figure 4 presents the scratch test results for the critical load evaluation. In this assessment, the onset of continuous coating spallation within the scratch track (L_{c2}) is conventionally established as the complete failure point [40], rendering L_{c2} the primary metric for the determination of the coating critical load. The single-AlCrSiN coating demonstrates a critical load of 63.0 N, which represents a 19.5% improvement over the corresponding value of 52.7 N obtained for the single-AlCrN coating. Importantly, the multi-AlCrSiN coating demonstrates an exceptional critical load of 87.8 N, establishing a clear positive correlation between the coating performance and both the layer count and total thickness. This performance enhancement originates from the fundamental advantages of the multilayer design: the gradual compositional transition between the layers optimizes the interface compatibility and stress distribution at the coating–substrate interface. The resulting improvement in the mechanical property

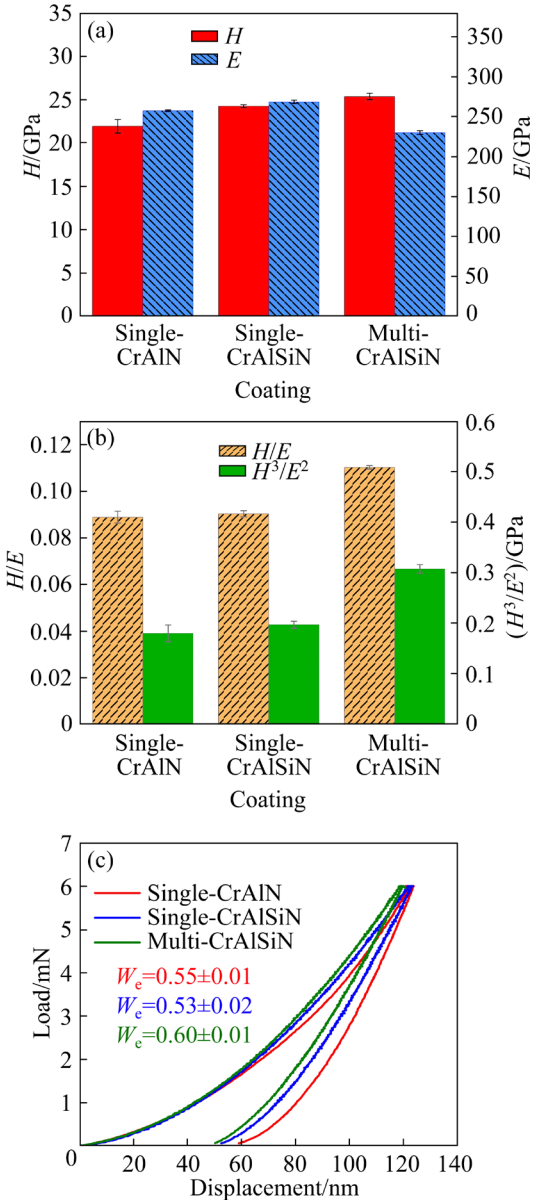

Fig. 3 (a) Surface hardness and elastic modulus; (b) H/E and H^3/E^2 values; (c) Load–displacement curves of three coatings

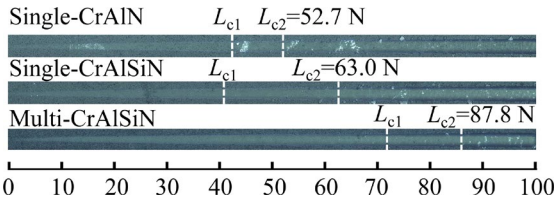

Fig. 4 Adhesion scratch test results of three coatings

gradation directly contributes to the superior load-bearing capacity of the composite coating.

3.3 High-temperature oxidation properties

Figures 5(a–c) present the surface morphology of the three coatings after oxidation at 850 °C. The single-AlCrN coating surface is completely covered with porous oxides, and EDS analysis reveals substantial O enrichment up to 60 at.% within the coating (Table 3). Conversely, the single-AlCrSiN and multi-AlCrSiN coatings possess numerous fine white particles on their surfaces after oxidation, with the multi-AlCrSiN variant exhibiting a substantially high particle density. Notably, after oxidation, both the Si-containing coatings retain a higher content of N than that of O. The EDS analysis confirms that the particles and coating surfaces comprise metal oxynitrides. The compositional analysis reveals negligible differences between the two Si-doped coatings; however, both exhibit minimal oxidation products on their surfaces.

The cross-sectional analysis in Figs. 5(d–f) reveals distinct oxidation behaviors. The single-AlCrN coating develops a thick, porous oxide layer that completely penetrates the coating, as evidenced by the progressive O concentration gradient from the surface to the substrate, indicating catastrophic oxidation failure. Conversely, both the single-AlCrSiN and multi-AlCrSiN coatings maintain their dense, layered structure without the substantial formation of oxide layers. Particularly, in the multi-AlCrSiN coating, the persistent N dominance over O throughout the cross-section confirms its superior oxidation resistance compared to the others, and the original multilayer architecture is maintained intact despite the high-temperature exposure.

Figures 6(a, b) present the GIXRD patterns of the three coatings before and after oxidation. In the as-deposited state, the multi-AlCrSiN coating exhibits a dual-phase composition comprising h-AlN and c-CrN. The use of an Al-rich target during deposition facilitates the dissolution of Al atoms into the c-CrN lattice, in which they substitute the Cr atoms. This substitution induces a measurable shift of the CrN diffraction peaks to large angles. However, the limited solubility of Al in c-CrN causes the precipitation of excess Al atoms from the lattice, forming h-AlN and resulting in a composite structure of c-CrN and h-AlN.

Comparative analysis reveals that the single-AlCrSiN coating contains a lower c-CrN content and higher h-AlN content than the multi-AlCrSiN coating, and AlN displays a preferred (100) orientation. Notably, the single-AlCrN coating has a considerably higher content of the h-Cr_2N phase [41],

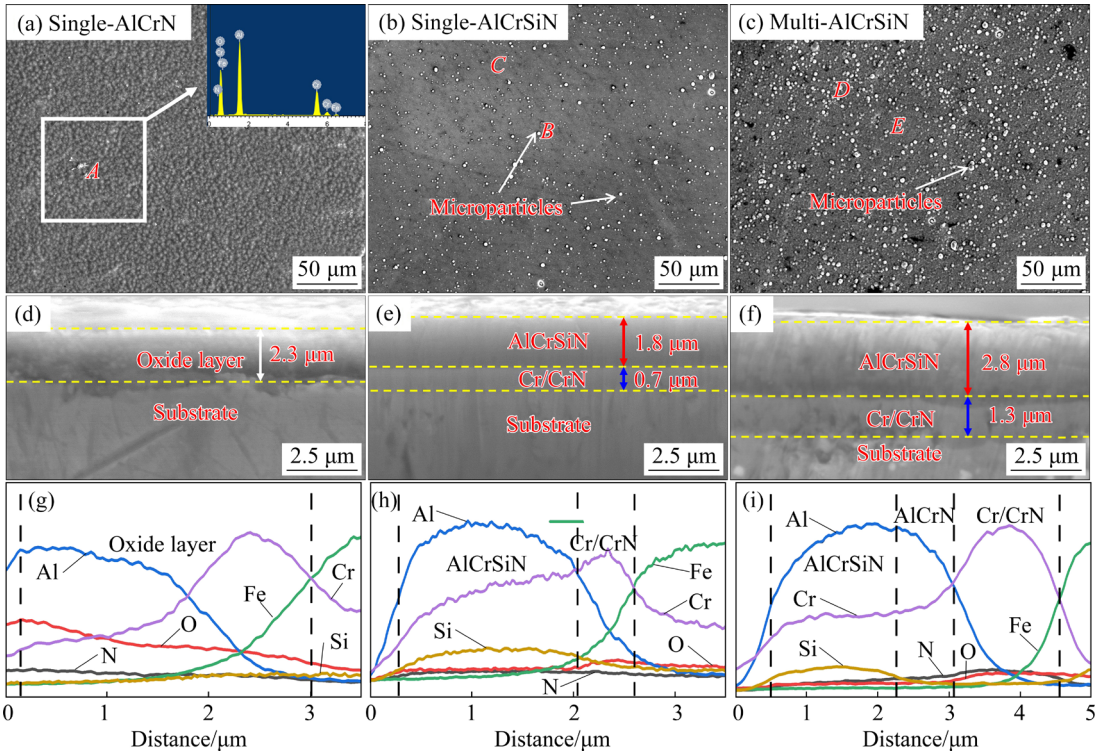

Fig. 5 SEM images (a–f) and corresponding EDS line scan results (g–i) of single-AlCrN (a, d, g), single-AlCrSiN (b, e, h), and multi-AlCrSiN (c, f, i) coatings after oxidation at 850 °C: (a–c) Surface morphology; (d–f) Cross-sectional morphology

Table 3 Element compositions of coating after oxidation at 850 °C for 8 h in different region in Fig. 5 (at.%)

Region	Cr	Al	Si	N	O	Fe
A	11.94	27.16	0.00	0.00	60.18	0.71
B	13.15	30.06	5.88	27.35	23.51	0.25
C	16.32	33.39	5.28	25.24	19.35	0.33
D	15.67	32.32	5.48	31.22	15.06	0.24
E	17.54	32.08	5.70	29.58	14.97	0.26

which possesses higher free energy and lower thermodynamic stability than c-CrN [42]. The absence of the detectable peaks of Si-containing phases in the XRD patterns indicates that Si exists either in a solid solution or as amorphous Si_3N_4 within the coating structure.

The phase composition of the coatings undergoes considerable changes after oxidation. For the single-AlCrN coating, complete oxidation occurs, transforming it into Cr_2O_3 and α-Al_2O_3 phases, with no remaining nitride phases detectable via XRD analysis. Conversely, Si introduction leads to a markedly different oxidation behavior in both single-layer and multilayer AlCrSiN coatings. These Si-containing coatings retain their original c-CrN and h-AlN phases after high-temperature oxidation and exhibit three key modifications: a substantial reduction in the Cr_2N diffraction intensity, a considerable enhancement of the CrN peaks, and the appearance of new c-$SiCr_3$ diffraction peaks that are absent before oxidation. According to QI et al [42], this phase evolution results from the thermal decomposition of the metastable Cr_2N phase into CrN and Cr at high temperatures, coupled with the dissociation of high-energy amorphous Si_3N_4. The liberated Si subsequently reacts with Cr to form the thermally stable $SiCr_3$ compound [18,43], as described by the following reaction equations:

$$Cr_2N \rightarrow CrN+Cr \quad (2)$$

$$Si_3N_4 \rightarrow 3Si+2N_2 \quad (3)$$

$$Si+3Cr \rightarrow Cr_3Si \quad (4)$$

Figures 6(c, d) present the TGA–DSC analysis results of the multi-AlCrSiN coating in both air and Ar atmospheres. In the air environment, the thermogravimetric curve reveals measurable mass loss during the heating stage, which is accompanied by a prominent exothermic peak in the DSC curve. This behavior originates from the thermal decomposition of amorphous Si_3N_4 and Cr_2N phases

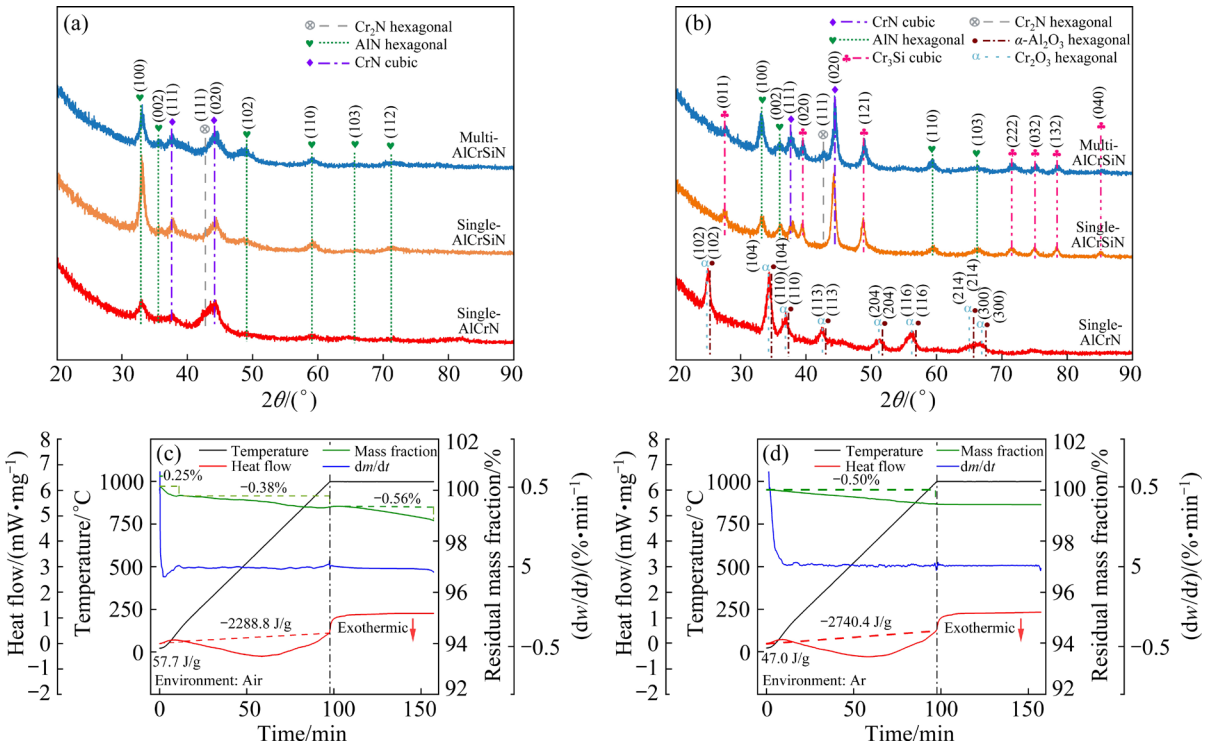

Fig. 6 (a, b) GIXRD patterns of coating in as-deposited state and after oxidation at 850 °C for 8 h, respectively; (c, d) TGA–DSC curves of coatings in air and Ar atmosphere, respectively

within the coating, releasing N_2 gas and consequently reducing the overall mass. During the subsequent isothermal holding at 1000 °C, continuous mass loss occurs through two concurrent mechanisms: progressive decomposition of CrN, and reaction of liberated N_2 with atmospheric O to form volatile nitrogen oxides that escape from the coating matrix. Conversely, the tests conducted in Ar atmosphere reveal a fundamentally different behavior. Although similar mass loss occurs during the heating stage because of the initial phase decomposition, the coating demonstrates excellent mass stability during the isothermal period at 1000 °C. This observation confirms the exceptional thermal stability of the multi-AlCrSiN coating in inert environments, in which oxidative degradation pathways are effectively suppressed.

XPS analysis was conducted on both the as-deposited and oxidized coatings (30 min and 8 h of oxidation) to investigate the evolution of the surface chemical states during oxidation. All the XPS spectra were charge-corrected using the adventitious carbon C 1s peak at 284.8 eV as a reference [44]. For the as-deposited coating (Fig. 7), the survey spectrum exhibits intense photoelectron peaks corresponding to Cr, Al, Si, and N, whereas only a weak O 1s signal is observed, indicating minimal surface oxidation. The core-level (N 1s, O 1s, Al 2p, Si 2p, and Cr 2p) spectra were deconvoluted using Gaussian–Lorentzian line functions to determine the chemical bonding states of the surface elements.

The N 1s spectrum of the as-deposited coating exhibits peaks related to three distinct components, namely, the Cr—N, Al—N, and O—N—Cr bonds at 396.8 [45], 397.4 [46], and 398.6 eV [47,48], respectively. The O 1s spectrum reveals two primary contributions from the Cr—O (531.1 eV [49,50]) and N—O (532.1 eV [51]) bonds. Al exists in two chemical environments: the Al—N bonds dissolved in the c-CrN lattice (73.5 eV [46]) and Al—N bonds in h-AlN (74.3 eV [46]). Notably, Si demonstrates dual bonding configurations, forming both Si—N (101.6 eV [25,52]) and Si—Cr (98.5 eV [49,53]) bonds. The Cr 2p spectrum illustrates a peak at 573.6 eV, which confirms the presence of Cr—Si bonds [53], exhibiting a chemical shift of 0.7 eV relative to Cr (574.3 eV [47]). Additionally, Cr exists in three other states: Cr_2N (574.5 eV [47]), CrN (575.8 eV [47,54]), and Cr—O (577.3 eV [55]).

Figure 8 presents the XPS spectra of the multi-AlCrSiN coating after oxidation at 850 °C for 0.5 and 8 h. The survey spectra obtained after 30 min of

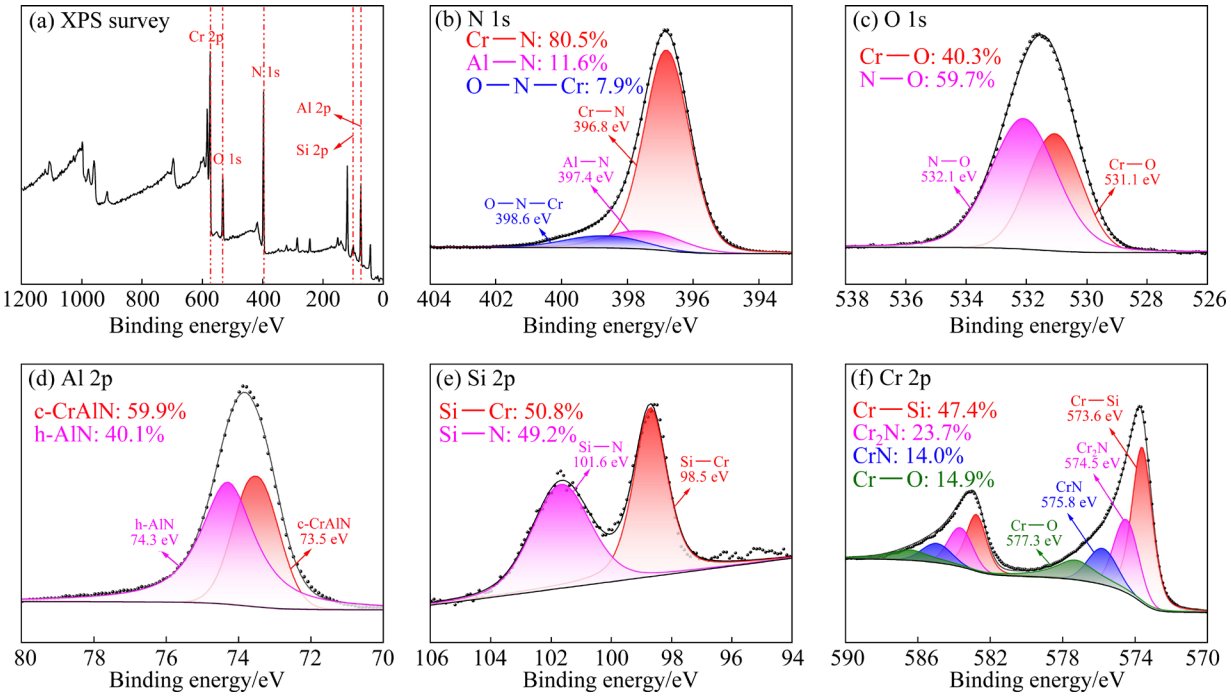

Fig. 7 XPS spectra of as-deposited AlCrSiN multilayer coating

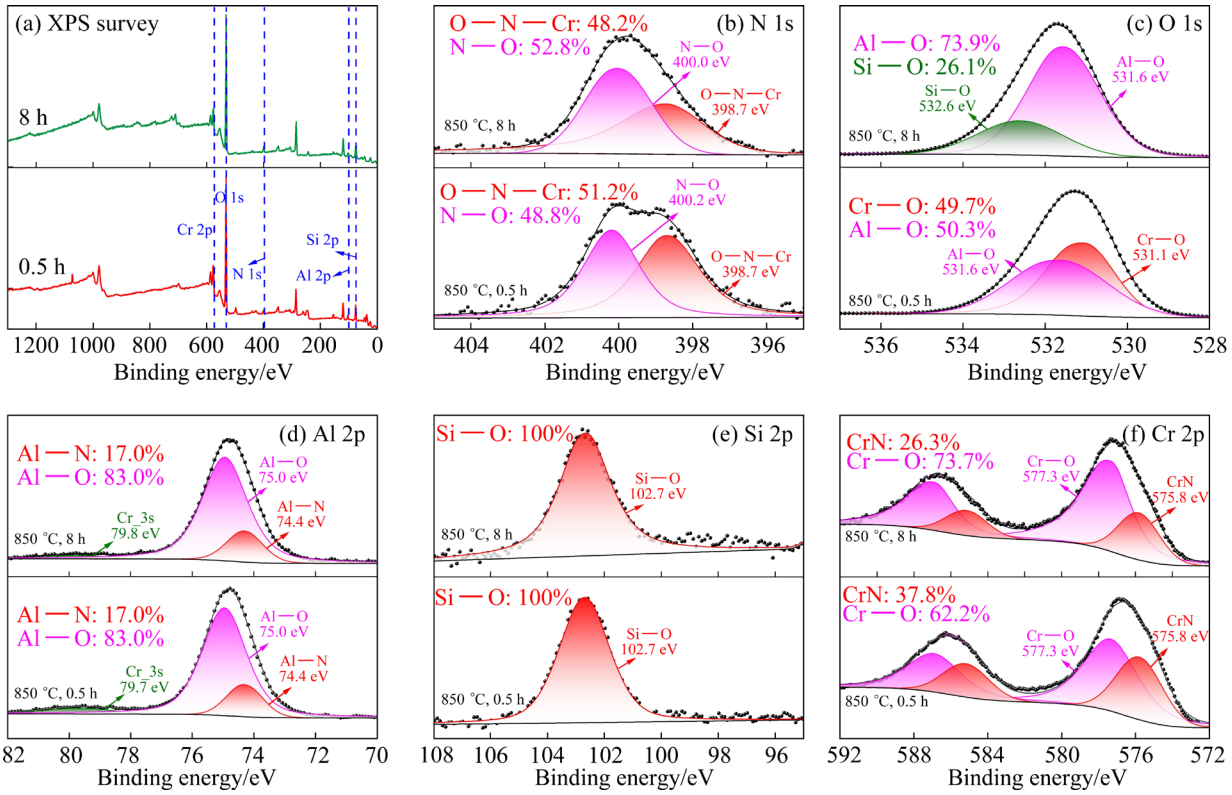

Fig. 8 XPS spectra of multi-AlCrSiN coating oxidized at 850 °C for 0.5 and 8 h

oxidation reveal three key aspects: a marked enhancement in the O 1s peak intensity, a corresponding reduction in the N 1s signal intensity, and persistent strong signals from Al 2p, Si 2p, and Cr 2p. Core-level spectral analysis demonstrates the complete transformation of the initial Cr—N and Al—N bonds into O—N—Cr and N—O configurations (398.6 eV [56]), whereas the O 1s spectrum confirms the simultaneous formation of Cr—O and Al—O bonds (531.6 eV [57]). Notably,

the Al 2p spectrum reveals the disappearance of Al—N bonds from the c-CrN lattice and the emergence of Al—O bonds (75.0 eV [58]). Furthermore, the Si 2p spectrum (102.7 eV [59]) suggests the complete oxidation of surface Si. The Cr 2p spectrum indicates the decomposition of Cr—Si bonds and Cr_2N, revealing substantial Cr—O bond formation and residual CrN retention.

A comparative analysis of the 8 h-oxidation samples indicates minimal changes in the survey spectra but reveals important progressive transformations in the chemical states. The N 1s spectrum demonstrates increased N—O bond formation through the conversion of the O—N—Cr bond, and the O 1s spectrum demonstrates an increasing Si—O bond contribution (532.6 eV [60]). Al maintains stable bonding configurations throughout the oxidation process, whereas Cr undergoes continuous transformation, during which the Cr—O bonds progressively replace the Cr—N bonds. These findings emphasize the dynamic characteristics of surface oxidation, during which rapid initial changes are followed by gradual bond conversion despite apparent spectral stability.

The oxidation behavior of the coating reveals a sequential transformation mechanism, in which Cr plays a dominant initial role in O capture owing to its higher adsorption activity than Al. In the as-deposited state, Al exists both as h-AlN and in a solid solution within cubic CrAlN (c-CrAlN), whereas Si primarily forms amorphous Si_3N_4 with additional Cr—Si bonding. During the initial 30 min of oxidation, the rapid decomposition of c-CrAlN, h-Cr_2N, and amorphous Si_3N_4 phases occurs, leading to the formation of Cr and Si oxides, together with the surface conversion of h-AlN to Al oxide. With extended oxidation time, the surface is progressively enriched with the Cr—O, N—O, and Si—O bonds, forming a highly stable composite oxide layer.

To elucidate the high-temperature oxidation mechanism, a detailed TEM characterization of the oxidized AlCrSiN multilayer coating was conducted. Figure 9(a) displays the bright-field image of the coating after 8 h of oxidation at 850 °C, revealing

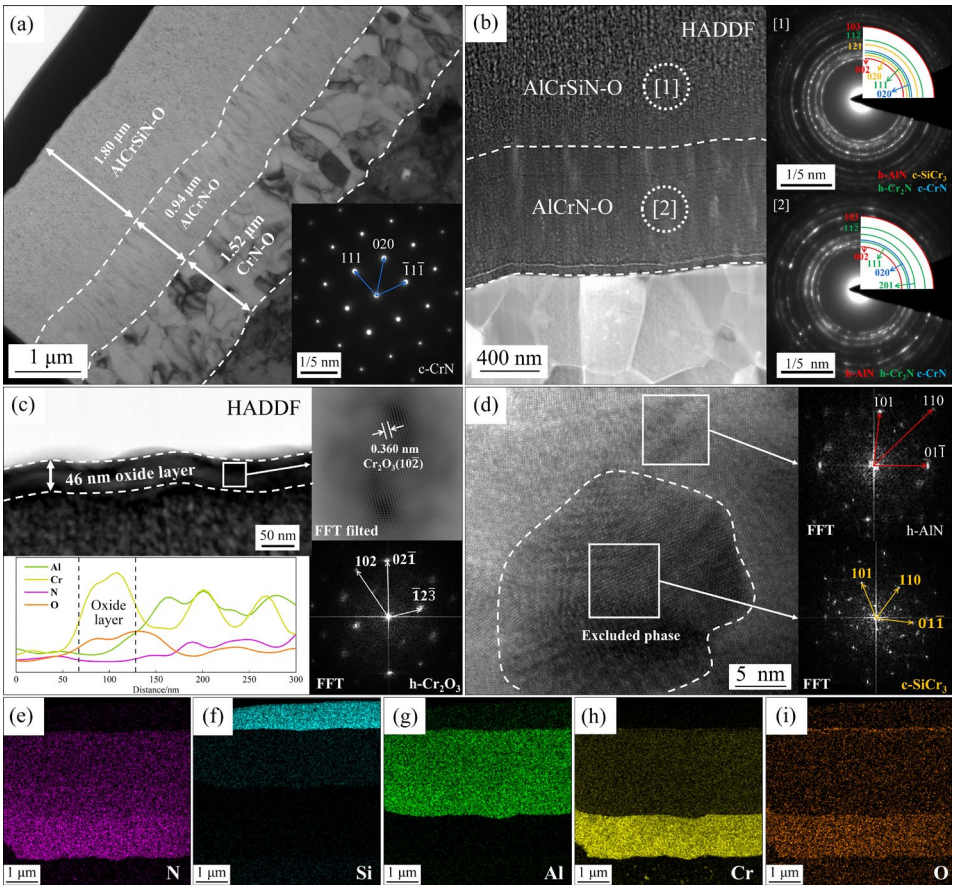

Fig. 9 Microstructures of multi-AlCrSiN coating after 8 h of oxidation: (a) Bright-field image; (b) HADDF image of entire coating; (c) HADDF, HRTEM, and EDS line scan images of oxide layer on coating surface; (d) HRTEM image of AlCrSiN layer; (e–i) EDS mapping of oxide coating

the retention of the original three-layer architecture. EDS mapping confirms the persistence of the CrN, AlCrN, and AlCrSiN layer sequence, although the metallic Cr base layer has completely oxidized. Post-oxidation, three notable changes are observed in the CrN layer: increased grain size with an equiaxed morphology, increase in the overall coating thickness, and complete transformation to c-CrN, as evidenced by the SAED patterns. This microstructural evolution results from the high-temperature decomposition of h-Cr_2N, accompanied by outward Cr diffusion and subsequent CrN recrystallization. Furthermore, EDS analysis reveals O dissolution in the c-CrN lattice.

Figure 9(b) presents the high-angle annular dark-field (HAADF) image of the AlCrSiN/AlCrN interface, demonstrating superior densification in the AlCrN layer compared to that in AlCrSiN, in which nanoscale precipitates are observed. Phase analysis via SAED reveals three coexisting phases in oxidized AlCrN (h-AlN, h-Cr_2N, and c-CrN), whereas the AlCrSiN layer additionally contains cubic $SiCr_3$ precipitates, as confirmed via the distinct diffraction rings.

The HAADF image in Fig. 9(c) reveals a 46 nm-thick surface oxide layer on AlCrSiN. The EDS line scans indicate the dominant presence of Cr and O, and complementary XPS data confirm the coexistence of Al—O and Cr—O bonds. Considering the isostructural characteristics of α-Al_2O_3 and Cr_2O_3 (space group $R\bar{3}c$), the HRTEM and FFT analyses collectively demonstrate the formation of a Cr-rich $(Cr,Al)_2O_3$ composite oxide layer at high temperatures. This dense nanoscale oxide film effectively prevents the inward diffusion of O, protecting the underlying coating from further oxidation. Figure 9(d) depicts the HRTEM image that reveals the $SiCr_3$ nanoparticles embedded in the AlN matrix, confirming the precipitation behavior of Si-containing phases during oxidation.

3.4 AIMD simulation

Figure 10 presents the atomic configurations and oxidation behaviors of $Cr_{0.5}Al_{0.5}N$, $Cr_{0.5-X}Al_{0.5}Si_XN$, and AlN systems after 2500 fs of molecular dynamics simulation at 1123 K (Fig. S8 in SI). The $Cr_{0.5}Al_{0.5}N$ system forms a mixed Cr–Al network oxide through outward metal diffusion, accompanied by vacancy-mediated inward penetration of O. Furthermore, the oxidation resistance of the $Cr_{0.5-X}Al_{0.5}Si_XN$ system is considerably improved owing to the Si-induced disruption of the continuous oxide networks. The AlN system exhibits unique oxidation characteristics: surface atoms form bonds with O, accompanied by the substitution of O atoms for N atoms in the surface lattice and the desorption of N_2O molecules as decomposition products, while maintaining excellent structural stability. These computational results quantitatively confirm the trend of the experimentally determined oxidation resistance: AlN>$Cr_{0.5-X}Al_{0.5}Si_XN$>$Cr_{0.5}Al_{0.5}N$.

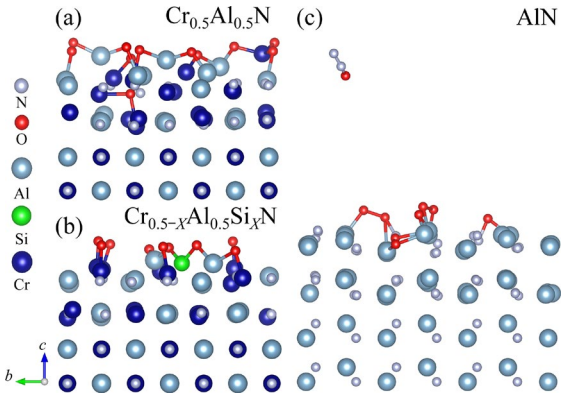

Fig. 10 Model structures of $Cr_{0.5}Al_{0.5}N$, $Cr_{0.5-X}Al_{0.5}Si_XN$, and AlN systems after simulation for 2500 fs

To quantitatively characterize the atomic migration behavior of the Al and Cr atoms in the three systems, we calculated the mean square displacement along the *z*-axis (MSD_z) for the atoms in the top two layers. The MSD_z is mathematically defined as follows:

$$MSD_z = \left|\vec{r}_z(t) - \vec{r}_z(0)\right|^2 \quad (5)$$

where $\vec{r}_z(t)$ denotes the *z*-coordinate of all particles at time t after the simulation starts, whereas $\vec{r}_z(0)$ denotes the *z*-coordinate of the particles in the initial configuration.

Figure 11 presents the MSD_z values for the atoms in the two top layers of each system. Owing to the lower atomic mass of Al (26.98 amu) than that of Cr (51.99 amu), the Al atoms exhibit considerably higher MSD_z values than the Cr atoms in the $Cr_{0.5}Al_{0.5}N$ system. This mass-dependent diffusion behavior leads to the formation of a composite oxide layer on the $Cr_{0.5}Al_{0.5}N$ surface, which is characterized by an Al-enriched upper region and a Cr-enriched lower region. Conversely, the $Cr_{0.5-X}Al_{0.5}Si_XN$ system demonstrates comparable

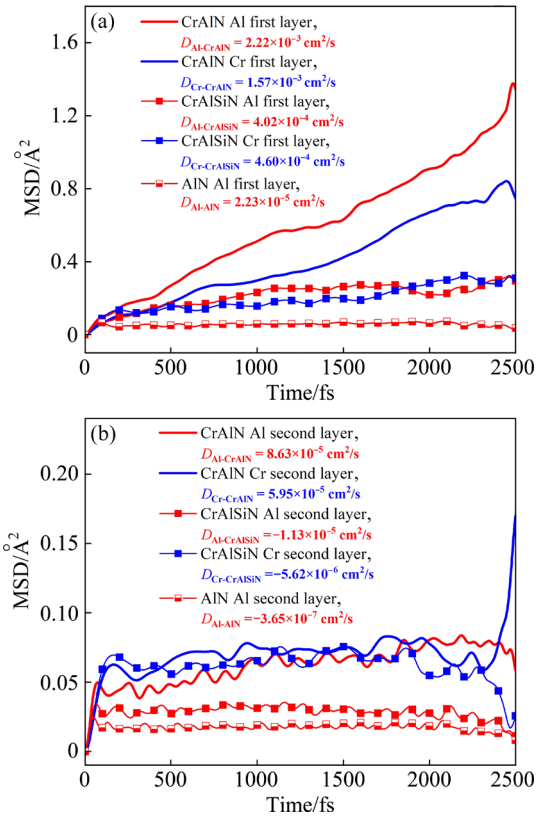

Fig. 11 MSD_z values of first and second layers of Cr and Al atoms in $Cr_{0.5}Al_{0.5}N$, $Cr_{0.5-X}Al_{0.5}Si_XN$, and AlN systems

MSD_z values for Al and Cr atoms, indicating a homogeneous Cr–Al mixed-oxide layer. Among the three systems, the AlN system exhibits the lowest MSD_z values, which is consistent with its superior structural stability during oxidation.

The analysis of MSD_z data enables the determination of the z-direction diffusion coefficients (D) for the atomic species in each layer. For the $Cr_{0.5}Al_{0.5}N$ system without Si incorporation, Al exhibited a surface diffusion coefficient of 2.22×10^{-3} cm²/s, whereas Cr demonstrated a lower value of 1.57×10^{-3} cm²/s. After the addition of Si in the $Cr_{0.5-X}Al_{0.5}Si_XN$ system, these diffusion coefficients substantially decreased to 4.02×10^{-4} and 4.60×10^{-4} cm²/s for Al and Cr, respectively, representing reductions of approximately 82% and 71% compared with the corresponding values of the Si-free system. The diffusion of surface Cr and Al atoms is considerably inhibited.

The AlN system exhibits exceptionally low Al diffusivity, demonstrating low values of 1% of the corresponding values of the $Cr_{0.5-X}Al_{0.5}Si_XN$ system. Comparative analysis indicates that h-AlN demonstrates the most constrained Al diffusion behavior among the three analyzed material systems. All the three systems display a consistent trend, where the second-layer metal atoms exhibit considerably lower diffusion coefficients than the surface atoms. Importantly, both the $Cr_{0.5-X}Al_{0.5}Si_XN$ and AlN systems display substantially reduced subsurface diffusion coefficients compared with the $Cr_{0.5}Al_{0.5}N$ system, confirming the effective suppression of the metal atom mobility. This diffusion inhibition primarily results from Si incorporation, which simultaneously restricts the outward diffusion of surface atoms and reduces the subsurface atomic mobility.

Figure 12 presents the radial distribution functions (RDFs) for the surface Cr, Al, Si, and N

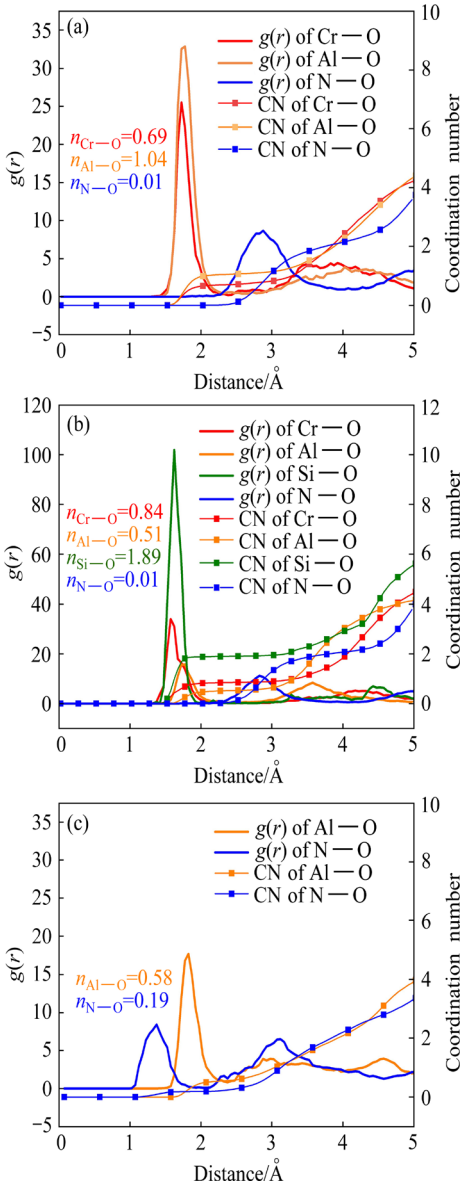

Fig. 12 RDF of surface atoms of $Cr_{0.5}Al_{0.5}N$, $Cr_{0.5-X}Al_{0.5}Si_XN$, and AlN systems (CN: Coordination number)

atoms interacting with O during oxidation in the three systems, revealing distinct bonding characteristics. In the $Cr_{0.5-X}Al_{0.5}Si_XN$ and $Cr_{0.5}Al_{0.5}N$ systems, the first-neighbor bonding peaks for Cr—O, Al—O, and Si—O appear between 1.5 and 2 Å, whereas the N—O peak is observed at considerably longer distances (2.5−3 Å), indicating unstable N—O bonding. Conversely, the AlN system demonstrates a markedly different behavior, exhibiting the N—O peak at 1.0—1.5 Å, which is substantially shorter than both the N—O distances in other systems, confirming the formation of stable covalent N—O bonds. This indicates a distinct bonding configuration in which the N atoms on the surface of AlN has higher chemical activity than those in the $Cr_{0.5-X}Al_{0.5}Si_XN$ and $Cr_{0.5}Al_{0.5}N$ systems.

Setting the threshold of the bond length as 2.3 Å, we quantified the number of O atoms bonded to the surface Cr, Al, Si, and N atoms within the 0−2.3 Å range across the three systems to characterize their surface bonding configurations. The $Cr_{0.5}Al_{0.5}N$ system exhibits 0.69 Cr—O bonds, 1.04 Al—O bonds, and 0.01 N—O bonds, demonstrating the superior O-bonding affinity of Al and the consequent formation of an Al oxide-dominated surface layer. Conversely, the $Cr_{0.5-X}Al_{0.5}Si_XN$ system exhibits a considerably different bonding behavior, featuring 0.85 Cr—O bonds, 0.53 Al—O bonds, 1.90 Si—O bonds, and 0.01 N—O bonds, revealing that Si addition promotes the formation of Cr oxide. Importantly, the AlN system displays unique bonding characteristics, exhibiting 0.58 Al—O bonds and 0.19 N—O bonds, representing a substantial enhancement in the N—O bonding compared with the other systems. This distinct behavior confirms that the N atoms on the AlN surface actively participate in the formation of stable N—O bonds at high temperatures.

Figures 13(a–c) present the valence electron differential charge density distributions of the three systems after 2500 fs of simulation, revealing distinct charge-transfer patterns during oxidation. In both the $Cr_{0.5}Al_{0.5}N$ and $Cr_{0.5-X}Al_{0.5}Si_XN$ systems, the surface Al atoms maintain relatively stable electron configurations, whereas the Cr atoms exhibit substantial electron transfer to O, indicating strong Cr—O bonding that facilitates the formation of a Cr-rich protective oxide layer at high temperatures. The $Cr_{0.5-X}Al_{0.5}Si_XN$ system exhibits additional charge redistribution, wherein the Si atoms form stable covalent bonds with both N and O through considerable electron sharing. This Si-induced pinning effect effectively restricts atomic diffusion, enhancing the oxidation resistance of the coating. Conversely, the AlN system exhibits a unique charge-transfer behavior, where O atoms substitute for lattice N while attracting electrons from both Al and neighboring N atoms, resulting in the formation of stable N—O covalent bonds that contribute to the exceptional thermal stability of the system.

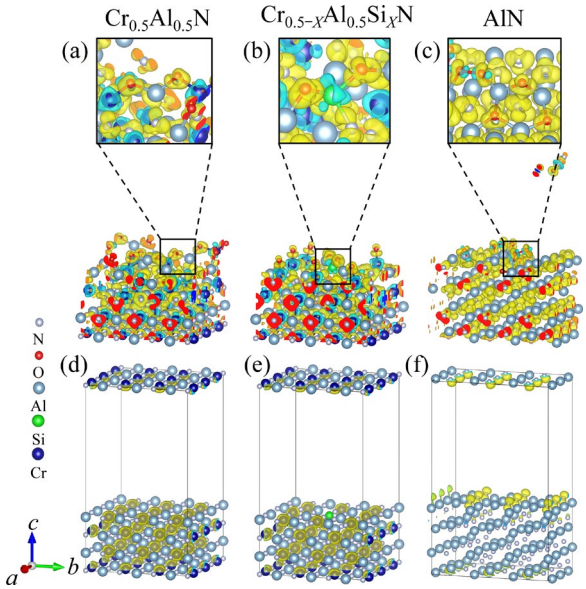

Fig. 13 $Cr_{0.5}Al_{0.5}N$, $Cr_{0.5-X}Al_{0.5}Si_XN$, and AlN systems: (a–c) Differential charge density (blue and yellow regions in differential charge density profile represent the loss and gain of electrons, respectively; electron equipotential surface is set as 0.02); (d–f) Spatiotemporal distribution of electrons at Fermi level between 0 and −1 eV (electron equipotential surface is set as 0.04)

Figures 13(d–f) display the spatiotemporal distribution of the Fermi-level electrons (energy range: −1 to 0 eV) in the three systems prior to oxidation, providing insights into their reactive sites. Because electrons near the Fermi level possess high chemical activity, their spatial distribution effectively indicates potential reaction centers. In both the $Cr_{0.5}Al_{0.5}N$ and $Cr_{0.5-X}Al_{0.5}Si_XN$ systems, these active electrons are predominantly localized around Cr atoms, as the 3d electrons of Cr exhibit a higher degree of localization and chemical activity near the Fermi level than those of Al. This electronic structure explains the superior chemical reactivity of Cr, which remains essentially unchanged upon Si addition. Consequently, O atoms preferentially bond with Cr in these systems. The AlN system presents a

markedly different electronic distribution, wherein Fermi-level electrons are primarily concentrated on the surface of N atoms. Owing to this configuration, N displays higher chemical activity than Al during oxidation, leading to two distinct reaction pathways: the preferential formation of N—O bonds with surface N and easier O substitution for surface N atoms in the lattice.

To further investigate the mechanism of the enhancement of oxidation resistance through Si addition, we dynamically tracked the characteristic bond length evolution during oxidation. Figure 14(a) presents the temporal variation of the surface Cr—O and subsurface Cr—N bond lengths in the $Cr_{0.5}Al_{0.5}N$ system. The simulation reveals that the Cr—N bonds undergo substantial elongation during the initial stages, reaching 4.40 Å by 360 fs (Fig. 14(c)), exceeding the stable bonding distance and resulting in bond rupture and vacancy formation. Concurrently, Cr—O distances progressively decrease as O atoms diffuse inward, achieving the characteristic Cr—O bond length of 1.80 Å at 1130 fs (Fig. 14(d)), which indicates stable Cr—O bond formation. Figure 14(b) demonstrates the distinct behavior in the $Cr_{0.5-X}Al_{0.5}Si_XN$ system, exhibiting the bond length evolution between Si and three species: subsurface N, surface N, and O atoms. Notably, the Si—O bonds rapidly form by 300 fs, whereas the subsurface Si—N bonds progressively elongate until complete dissociation at 380 fs. Crucially, the surface Si—N bonds remain stable throughout the entire 2500 fs simulation, in which the Si atoms are persistently pinned on the system surface.

The AIMD simulation results reveal the distinct oxidation mechanisms of the three material systems. In the $Cr_{0.5}Al_{0.5}N$ system, the surface metal atoms bond with O, inducing the outward diffusion of N and vacancy formation. These vacancies facilitate the inward diffusion of O, initiating oxidation. Owing to their lower atomic mass, Al atoms exhibit higher diffusivity than Cr atoms, leading to the development of a stratified oxide layer comprising an Al-rich outer region and a Cr-rich inner zone.

The AIMD simulation results reveals the distinct oxidation mechanisms of the three material systems. In the $Cr_{0.5}Al_{0.5}N$ system, the surface metal atoms bond with O, inducing the outward diffusion of N and vacancy formation. These vacancies facilitate the inward diffusion of O, initiating oxidation. Owing to their lower atomic mass, Al atoms exhibit higher diffusivity than Cr atoms, leading to the development of a stratified oxide layer comprising an Al-rich outer region and a Cr-rich inner zone.

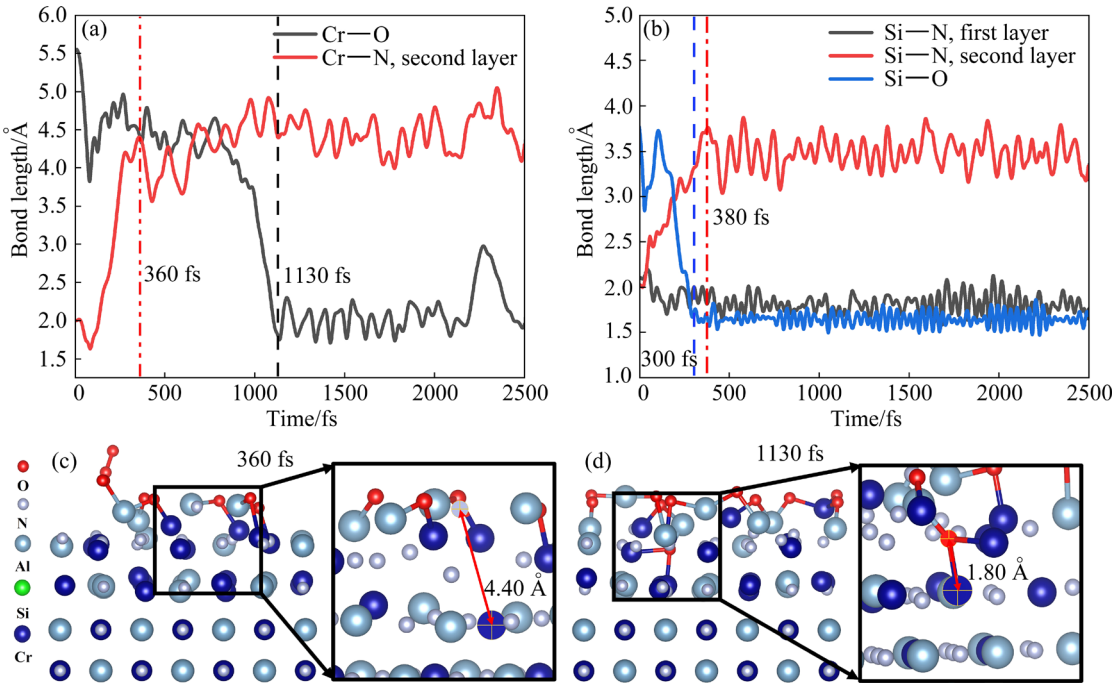

Fig. 14 (a) Tracking of Cr—O and Cr—N characteristic bond lengths of $Cr_{0.5}Al_{0.5}N$ system; (b) Tracking of Si—N and Si—O characteristic bond lengths of $Cr_{0.5-X}Al_{0.5}Si_XN$ system; (c) Vacancy formation model of N atoms in $Cr_{0.5}Al_{0.5}N$ system for 360 fs; (d) Internal diffusion model of O atoms in $Cr_{0.5}Al_{0.5}N$ system for 1130 fs

The $Cr_{0.5-X}Al_{0.5}Si_XN$ system demonstrates a different behavior, where the Si atoms form stable covalent bonds with both N and O. The persistence of the surface Si—N bonds, which are resistant to rupturing, anchors the Si atoms on the surface. This pinning effect effectively suppresses both the outward diffusion of Cr and Al atoms and the inward penetration of O, inhibiting the formation of the composite oxide layer. Consequently, O preferentially bonds with the more reactive Cr atoms, yielding a Cr-dominated Cr—Al monolayer oxide.

Conversely, the AlN system displays minimal O-bonding capability compared with the other systems. During oxidation, O atoms are incorporated into the AlN lattice, whereas N escapes as N_2O molecules from the surface. Importantly, the AlN surface maintains its original crystal structure, and O adsorption is limited to surface N and Al sites. This unique behavior underlies the exceptional oxidation resistance of the system.

3.5 Oxidation mechanism of coatings

The combined experimental and AIMD simulation results are presented in Fig. 15 to elucidate the distinct oxidation mechanisms of the single-AlCrN and multi-AlCrSiN coatings. In the Si-free single-AlCrN coating, the simultaneous outward diffusion of Al and Cr atoms at high temperatures generates surface vacancies that facilitate the O penetration of the coating. The differential diffusion rates between the lighter Al atoms and the heavier Cr atoms lead to the formation of a stratified oxide structure comprising an Al-enriched outer layer and a Cr-enriched inner layer.

Although previous research [10,18] has demonstrated that AlCrSiN coatings comprising a N content of 50 at.% develop similar Al-rich outer layers and Cr-rich inner oxide layers at high temperatures, the current demonstrates that reducing the N content to <50 at.% inverts this stratification, yielding a Cr-rich outer layer/Al-rich inner oxide configuration. Si incorporation induces considerable microstructural modifications in the multi-AlCrSiN coating, resulting in surface amorphization. During high-temperature exposure, the amorphous Si_3N_4 and Cr_2N phases decompose, liberating Cr atoms that diffuse outward, while the released Si preferentially forms $SiCr_3$ nanoparticles that effectively immobilize Cr. This nanoparticle formation mechanism enhances the thermal stability of the coating. Concurrently, insufficiently nitrided surface Cr atoms react with O to generate a Cr-enriched $(Cr,Al)_2O_3$ composite oxide layer. The internal structure of the coating exhibits contrasting thermal stabilities, and h-AlN demonstrates superior stability to cubic Cr(AlSi)N at high temperatures. The highly reactive 3d electrons of Cr in the Cr(AlSi)N phase promote preferential Cr—O bonding. The exceptional bonding stability of Si, via Si—N and Si—O interactions, leads to the generation of a surface pinning effect that simultaneously obstructs the ingression of O and restricts the outward diffusion of Cr and Al atoms. Ultimately, these mechanisms lead to the formation of a dense, nanoscale Cr-rich $(Cr,Al)_2O_3$ surface oxide film that effectively protects the underlying coating from further oxidation.

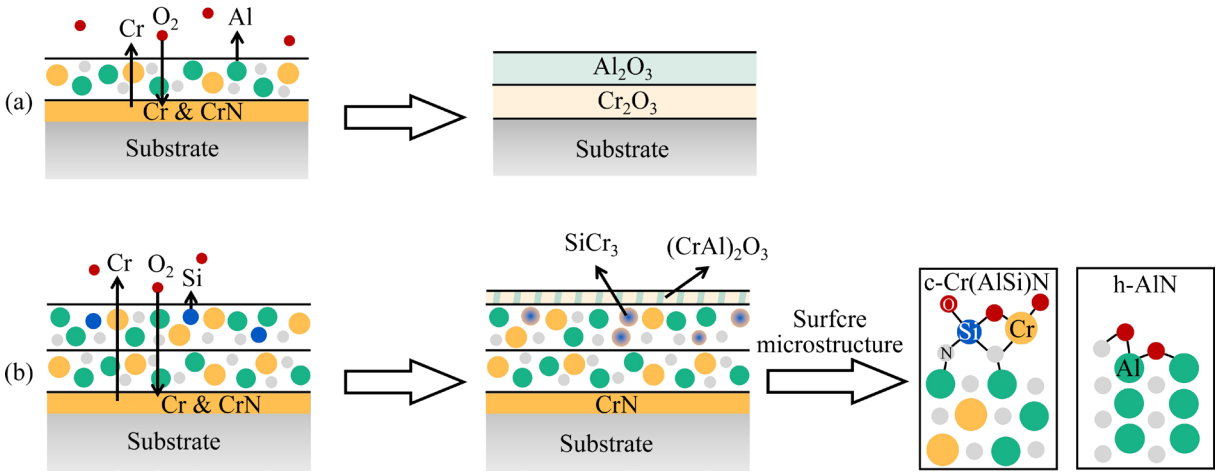

Fig. 15 Oxidation mechanism of single-AlCrN (a) and multi-AlCrSiN (b) composite coatings

4 Conclusions

(1) Si incorporation increased the hardness of the multi-AlCrSiN coating by 15% (26 GPa) and the critical load by 67% (87.8 N), considerably improving the interfacial bonding and mechanical performance compared with those of the single-AlCrN coating.

(2) At 850 °C, in air, Cr_2N and Si_3N_4 in the coating decomposed into stable CrN and $SiCr_3$, whereas incompletely nitrided Cr atoms preferentially reacted with O to form a nanoscale Cr-rich $(CrAl)_2O_3$ protective layer, effectively blocking O diffusion.

(3) AIMD simulations revealed that Cr atoms exhibited higher chemical activity than Al atoms, preferentially forming a Cr-rich oxide layer. Si atoms created a pinning effect, suppressing metal/O diffusion. This dual mechanism enhanced the oxidation resistance, and the simulations closely matched the experimental results.

CRediT authorship contribution statement

Ji-yuan LIU: Conceptualization, Methodology, Investigation, Data curation, Visualization, Writing − Original draft; **Shu-bing HU:** Supervision, Methodology, Funding acquisition, Project administration, Writing − Review & editing; **Bo PENG:** Formal analysis, Investigation; **Jing-jing TIAN:** Formal analysis, Investigation; **Si-qi ZENG:** Writing − Review & editing, Investigation; **Hai-xin CHANG:** Resources; **Hong-ya LI:** Formal analysis, Investigation; **Jin-ke YU:** Formal analysis, Investigation; **Fei GUO:** Resources.

Declaration of competing interest

The authors declare that they have no known competing financial interests or personal relationships that could have appeared to influence the work reported in this paper.

Acknowledgments

This work was financially supported by the National Science and Technology Major Project (No. 2024ZD1404705). The authors thank the Analytical and Testing Center of Huazhong University of Science and Technology and the State Key Laboratory of Materials Processing and Die & Mold Technology for characterizations. The computation is completed in the HPC Platform of Huazhong University of Science and Technology.

Supporting Information

Supporting Information in this paper can be found at: https://tnmsc.csu.edu.cn/download/14-p0552-2024-1211-Supporting_Information.pdf.

References

[1] EDIS R, SINMAZCELIK T, ERTURK A T. Measuring applied force and energy consumption in deep drawing die sets: An experimental and numerical analysis of CrN and CrTiN PVD coating effects [J]. Measurement, 2024, 224: 113841.

[2] GAO Ying, CAI Fei, LU Xin, XU Wei, ZHANG Ce, ZHANG Jia-zhen, QU Xuan-Hui. Design of cycle structure on microstructure, mechanical properties and tribology behavior of AlCrN/AlCrSiN coatings [J]. Ceramics International, 2022, 48(9): 12255−12270.

[3] LIU Ming-ze, SANG Bao-guang, HAO Chun-lei, CHEN Guo-xin, YAN Jin. Thermal fatigue life prediction method for die casting mold steel based on the cooling cycle [J]. Journal of Materials Processing Technology, 2023, 321: 118131.

[4] HU Ke, HU Shu-bing, ZENG Si-qi, PENG Bo, XIONG Xue-song, WANG Wen-kai, CHENG Guang-kun. The effect of surface treatment on the corrosion behavior of pure Ta sheet in an equimolar NaCl−KCl melt at 850 °C in air, Part 2: Diamond film, TaC film, Ta-Si coating and Ta−Si−Al coating [J]. Corrosion Science, 2019, 154: 11−27.

[5] ICHOU H, ARROUSSE N, BERDIMURODOV E, ALIEV N. Exploring the advancements in physical vapor deposition coating: A review [J]. Journal of Bio- and Tribo-Corrosion, 2023, 10(1): 3.

[6] WARCHOLINSKI B, GILEWICZ A, MYSLINSKI P, DOBRUCHOWSKA E, MURZYNSKI D. Structure and properties of AlCrN coatings deposited using cathodic arc evaporation [J]. Coatings, 2020, 10(8): 793.

[7] RAMÍREZ-REYNA F O, RODRÍGUEZ-CASTRO G A, FIGUEROA-LÓPEZ U, MORÓN R C, ARZATE-VÁZQUEZ I, MENESES-AMADOR A. Effect of nitriding pretreatment on adhesion and tribological properties of AlCrN coating [J]. Materials Letters, 2021, 284: 128931.

[8] XIE Jing, WANG Jian-chuan, ZENG Fang-fang, HAN Bo, GUO Fang-yu, QIU Lian-chang, DU Yong. Oxidation resistance of TiSiN and AlCrN hard-coatings: Ab initio calculations and experiments [J]. Applied Surface Science, 2023, 616: 156459.

[9] CHEN Wang-lin, HU Te, HONG Yue, ZHANG Dao-da, MENG Xian-na. Comparison of microstructures, mechanical and tribological properties of arc-deposited AlCrN, AlCrBN and CrBN coatings on Ti−6Al−4V alloy [J]. Surface and Coatings Technology, 2020, 404: 126429.

[10] XIAO Bai-jun, ZHANG Teng-fei, GUO Zhu, LI Zhou, FAN Bin, CHEN Gan-xin, XIONG Zhi-hong, WANG Qi-min. Mechanical, oxidation, and cutting properties of AlCrN/AlTiSiN nano-multilayer coatings [J]. Surface and Coatings Technology, 2022, 433: 128094.

[11] GENG Dong-sen, LI Hai-qing, CHEN Zi-liang, XU Yu-xiang, WANG Qi-min. Microstructure, oxidation behavior and tribological properties of AlCrN/Cu coatings deposited by a hybrid PVD technique [J]. Journal of Materials Science & Technology, 2022, 100: 150−160.

[12] TIAN Jin-lian, HU Chun, CHEN Li, LOU Yu-min, ZHAO Ning-ning. Structure, mechanical and thermal properties of Y-

doped CrAlN coatings [J]. Transactions of Nonferrous Metals Society of China, 2021, 31(9): 2740−2749.

[13] LIU Y, LIU H D, PELENOVICH V, WAN Q, GUO J L, CHEN Y M, ZHANG J, XUE L J, LI Z G, YANG B. Influences of modulation period on structure and properties of AlTiSiN/AlCrSiN nanocomposite multilayer coatings [J]. Vacuum, 2021, 193: 110516.

[14] WU Zheng-tao, HUAN Jing, GENG Dong-sen, YE Rong-li, WANG Qi-min. Investigation on plastic deformation of arc-evaporated AlCrSiN and AlCrSiON nanocomposite films by indentation [J]. Surface and Coatings Technology, 2022, 441: 128570.

[15] CAI Fei, GAO Ying, ZHANG Shi-hong, ZHANG Lin, WANG Qi-min. Gradient architecture of Si containing layer and improved cutting performance of AlCrSiN coated tools [J]. Wear, 2019, 424/425: 193−202.

[16] POLCAR T, CAVALEIRO A. High-temperature tribological properties of CrAlN, CrAlSiN and AlCrSiN coatings [J]. Surface and Coatings Technology, 2011, 206(6): 1244−1251.

[17] ZHANG Quan, XU Yu-xiang, ZHANG Teng-fei, WU Zheng-tao, WANG Qi-min. Tribological properties, oxidation resistance and turning performance of AlTiN/AlCrSiN multilayer coatings by arc ion plating [J]. Surface and Coatings Technology, 2018, 356: 1−10.

[18] JÄGER N, MEINDLHUMER M, ZITEK M, SPOR S, HRUBY H, NAHIF F, JULIN J, ROSENTHAL M, KECKES J, MITTERER C, DANIEL R. Impact of Si on the high-temperature oxidation of AlCr(Si)N coatings [J]. Journal of Materials Science & Technology, 2022, 100: 91−100.

[19] JÄGER N, MEINDLHUMER M, SPOR S, HRUBY H, JULIN J, STARK A, NAHIF F, KECKES J, MITTERER C, DANIEL R. Microstructural evolution and thermal stability of AlCr(Si)N hard coatings revealed by in-situ high-temperature high-energy grazing incidence transmission X-ray diffraction [J]. Acta Materialia, 2020, 186: 545−554.

[20] CHANG Y Y, AMRUTWAR S. Effect of plasma nitriding pretreatment on the mechanical properties of AlCrSiN-coated tool steels [J]. Materials, 2019, 12(5): 795.

[21] CHANG Chi-lung, HUANG Chun-hong, LIN Ching-yen, YANG Fu-chi, TANG Jian-fu. Mechanical properties of amorphous and crystalline CrN/CrAlSiN multilayer coating fabricated using HPPMS [J]. Surfaces and Interfaces, 2022, 31: 102064.

[22] LIU Zhe-ren, XU Yu-xiang, PENG Bin, WEI Wei, CHEN Li, WANG Qi-min. Structure and property optimization of Ni-containing AlCrSiN coatings by nano-multilayer construction [J]. Journal of Alloys and Compounds, 2019, 808: 151630.

[23] TANG Jian-fu, HUANG Chun-hong, LIN Ching-yen, YANG Fu-chi, CHANG Chi-lung. Effects of substrate rotation speed on structure and adhesion properties of CrN/CrAlSiN multilayer coatings prepared using high-power impulse magnetron sputtering [J]. Coatings, 2020, 10(8): 742.

[24] AZIZPOUR A, HAHN R, KLIMASHIN F F, WOJCIK T, POURSAEIDI E, MAYRHOFER P H. Deformation and cracking mechanism in CrN/TiN multilayer coatings [J]. Coatings, 2019, 9(6): 363.

[25] POLCAR T, CAVALEIRO A. High temperature properties of CrAlN, CrAlSiN and AlCrSiN coatings—Structure and oxidation [J]. Materials Chemistry and Physics, 2011, 129(1/2): 195−201.

[26] GUO Fang-yu, WANG Jian-chuan, DU Yong, WANG Jiong, SHANG Shun-li, LI Song-lin, CHEN Li. First-principles study of adsorption and diffusion of oxygen on surfaces of TiN, ZrN and HfN [J]. Applied Surface Science, 2018, 452: 457−462.

[27] ZHU Long-peng, WANG Jiong, DONG Chen-chen, SHANG Shun-li, DU Yong, LIU Zi-kui, ZHANG Shu-yan. Understanding the surface adsorption and oxidation of cubic $Cr_{0.5}Al_{0.5}N$ by first-principles calculations [J]. Computational Materials Science, 2021, 196: 110518.

[28] GUO Fang-yu, HOLEC D, WANG Jian-chuan, LI Song-lin, DU Yong. Impact of V, Hf and Si on oxidation processes in Ti–Al–N: Insights from ab initio molecular dynamics [J]. Surface and Coatings Technology, 2020, 381: 125125.

[29] KRESSE G, FURTHMÜLLER J. Efficient iterative schemes for ab initio total-energy calculations using a plane-wave basis set [J]. Physical Review B, 1996, 54(16): 11169−11186.

[30] KRESSE G, HAFNER J. Ab initio molecular dynamics for open-shell transition metals [J]. Physical Review B, 1993, 48(17): 13115−13118.

[31] KRESSE G, JOUBERT D. From ultrasoft pseudopotentials to the projector augmented-wave method [J]. Physical Review B, 1999, 59(3): 1758−1775.

[32] PERDEW J P, CHEVARY J A, VOSKO S H, JACKSON K A, PEDERSON M R, SINGH D J, FIOLHAIS C. Atoms, molecules, solids, and surfaces: Applications of the generalized gradient approximation for exchange and correlation [J]. Physical Review B, 1992, 46(11): 6671−6687.

[33] PERDEW J P, BURKE K, ERNZERHOF M. Generalized gradient approximation made simple [J]. Physical Review Letters, 1996, 77(18): 3865−3868.

[34] GUO Fang-yu, WANG Jian-chuan, DU Yong, HOLEC D, OU Peng-fei, ZHOU Hao, CHEN Li, KONG Yi. Structural evolution of oxygen on the surface of TiAlN: Ab initio molecular dynamics simulations [J]. Applied Surface Science, 2019, 470: 520−525.

[35] MONKHORST H J, PACK J D. Special points for Brillouin-zone integrations [J]. Physical Review B, 1976, 13(12): 5188−5192.

[36] LEYLAND A, MATTHEWS A. On the significance of the H/E ratio in wear control: A nanocomposite coating approach to optimised tribological behaviour [J]. Wear, 2000, 246(1/2): 1−11.

[37] CHEN Xin-jie, DU Yao, CHUNG Y W. Commentary on using H/E and H^3/E^2 as proxies for fracture toughness of hard coatings [J]. Thin Solid Films, 2019, 688: 137265.

[38] YANG Wei, SHEN Jian-xiao, WANG Zhen-yu, MA Guan-shui, KE Pei-ling, WANG Ai-ying. Mechanical and electrochemical properties of $(MoNbTaTiZr)_{1-x}N_x$ high-entropy nitride coatings [J]. Journal of Materials Science & Technology, 2025, 208: 78−91.

[39] GADGE M, CHINCHANIKAR S. Characterization of pre- and/or post-treated PVD-AlTiN coating: Nanohardness, modulus of indentation and percent elastic portion of the nanoindentation [J]. Materials Today: Proceedings, 2021, 46: 8386−8392.

[40] TANG J F, CHEN I H, LU B R, CHANG C L. Effect of bias voltages and interlayer design on microstructure, mechanical properties, and adhesion performance of AlCrSiN coatings deposited using HiPIMS [J]. Surface and Coatings Technology, 2024, 480: 130618.

[41] WARCHOLINSKI B, GILEWICZ A, KUPRIN A S, KOLODIY I V. Structure and properties of CrN coatings formed using cathodic arc evaporation in stationary system [J]. Transactions of Nonferrous Metals Society of China, 2019, 29(4): 799−810.

[42] QI Zheng-bing, LIU Bi-hua, WU Zheng-tao, ZHU Fang-ping, WANG Zhou-cheng, WU Chong-hu. A comparative study of

the oxidation behavior of Cr_2N and CrN coatings [J]. Thin Solid Films, 2013, 544: 515−520.
[43] SAMSONOV G V, LAVRENKO V A, GLEBOV L A. Oxidation of chromium disilicide in oxygen [J]. Soviet Powder Metallurgy and Metal Ceramics, 1974, 13(1): 36−38.
[44] CAO Hong-shuai, LIU Fu-jia, LI Hao, LUO Wen-zhong, QI Fu-gang, LU Li-wei, ZHAO Nie, OUYANG Xiao-ping. Effect of bias voltage on microstructure, mechanical and tribological properties of TiAlN coatings [J]. Transactions of Nonferrous Metals Society of China, 2022, 32(11): 3596−3609.
[45] LIPPITZ A, HÜBERT T. XPS investigations of chromium nitride thin films [J]. Surface and Coatings Technology, 2005, 200(1/2/3/4): 250−253.
[46] VYAS A, ZHOU Z F, SHEN Y G. Effect of aluminum contents on sputter deposited CrAlN thin films [J]. IOP Conference Series: Materials Science and Engineering, 2018, 307: 012079.
[47] BARSHILIA H C, SELVAKUMAR N, DEEPTHI B, RAJAM K S. A comparative study of reactive direct current magnetron sputtered CrAlN and CrN coatings [J]. Surface and Coatings Technology, 2006, 201(6): 2193−2201.
[48] DU Jian-wei, YAN Xiang-yu, CHEN Li, YUE Jian-ling, DU Yong. Enhancing corrosion behavior of CrN coating through oxygen incorporation: Experimental and theoretical analyses [J]. Ceramics International, 2024, 50(15): 27380−27388.
[49] JILEK M, CSELLE T, HOLUBAR P, MORSTEIN M, VEPREK-HEIJMAN M G J, VEPREK S. Development of novel coating technology by vacuum arc with rotating cathodes for industrial production of nc-$(Al_{1-x}Ti_x)$N/a-Si_3N_4 superhard nanocomposite coatings for dry, hard machining [J]. Plasma Chemistry and Plasma Processing, 2004, 24(4): 493−510.
[50] IKEMOTO I, ISHII K, KINOSHITA S, KURODA H, ALARIO FRANCO M A, THOMAS J M. X-ray photoelectron spectroscopic studies of CrO_2 and some related chromium compounds [J]. Journal of Solid State Chemistry, 1976, 17(4): 425−430.
[51] PASHUTSKI A, FOLMAN M. Low temperature XPS studies of NO and N_2O adsorption on Al(100) [J]. Surface Science, 1989, 216(3): 395−408.
[52] RAI D K, PANCHAL A K, SUTAR D S, SOLANKI C S, BALASUBRAMANIAM K R. Mechanism for formation of ultra thin SiN_x on a-Si—XPS and FTIR studies [C]//2015 IEEE 42nd Photovoltaic Specialist Conference (PVSC). New Orleans, LA, USA: IEEE, 2015: 1−6.
[53] JOHANSSON L I, HÅKANSSON K L, KARLSSON U O, CHRISTENSEN A N. Core level photoemission study of Cr_3Si(100) [J]. Surface Science, 1991, 251/252: 101−107.
[54] EMERY C, CHOURASIA A R, YASHAR P. A study of CrN*x* thin films by X-ray photoelectron spectroscopy [J]. Journal of Electron Spectroscopy and Related Phenomena, 1999, 104(1/2/3): 91−97.
[55] KADARI A, SCHEMME T, KADRI D, WOLLSCHLÄGER J. XPS and morphological properties of Cr_2O_3 thin films grown by thermal evaporation method [J]. Results in Physics, 2017, 7: 3124−3129.
[56] WEI Jian-jun, XUE Qun-ji. Effects of synthetic additives on the friction and wear properties of a Cr_2O_3 coating [J]. Wear, 1994, 176(2): 213−216.
[57] IATSUNSKYI I, KEMPIŃSKI M, JANCELEWICZ M, ZAŁĘSKI K, JURGA S, SMYNTYNA V. Structural and XPS characterization of ALD Al_2O_3 coated porous silicon [J]. Vacuum, 2015, 113: 52−58.
[58] KING D E, SWARTZ W E. Variable-angle X-ray photoelectron spectroscopic determination of the thickness of the oxide layer on aluminum metal: An advanced undergraduate laboratory experiment [J]. Journal of Chemical Education, 1987, 64(11): 981.
[59] NGUYEN T P, LEFRANT S. XPS study of SiO thin films and SiO-metal interfaces [J]. Journal of Physics: Condensed Matter, 1989, 1(31): 5197−5204.
[60] MILLER M L, LINTON R W. X-ray photoelectron spectroscopy of thermally treated silica (SiO_2) surfaces [J]. Analytical Chemistry, 1985, 57(12): 2314−2319.

AlCrSiN 多层涂层氧化机理的多尺度实验与第一性原理分子动力学研究

刘纪元[1,2]，胡树兵[1,2]，彭 博[1,2]，田静静[1,2]，曾思琪[3]，常海欣[1,2]，李鸿亚[1,2]，余金科[1,2]，郭 飞[4,5]

1. 华中科技大学 材料成形与模具技术全国重点实验室，武汉 430074；
2. 华中科技大学 材料科学与工程学院，武汉 430074；
3. 江西省科学院 应用物理研究所，南昌 330096；
4. 广西科技大学 电子工程学院，柳州 545006；
5. 广西科技大学 柳州市新能源汽车动力锂电池重点实验室，柳州 545006

摘 要：采用复合多弧离子镀与高功率脉冲磁控溅射技术，开发了新型 AlCrSiN/AlCrN/CrN/Cr 多层涂层。该多层结构设计显著提高了基体−涂层的相容性，临界载荷达到 87.8 N。硅掺杂诱导纳米晶化与非晶化转变，使硬度提高至 26 GPa。高温环境下形成的纳米级富 Cr 的$(Cr,Al)_2O_3$层有效抑制了氧扩散。涂层经历了独特的相变过程：Cr_2N 与非晶 Si_3N_4 转化为弥散分布的 $SiCr_3$ 纳米颗粒，不仅稳定了 Cr 原子，还抑制了其外扩散行为。基于第一性原理的分子动力学模拟表明，Cr 原子比 Al 原子具有更高的化学活性和捕氧能力，而 Si 原子通过钉扎氧化表面形成扩散势垒，显著提升了涂层的抗氧化性能。

关键词：物理气相沉积；AlCrSiN 涂层；氧化；AIMD 模拟

(Edited by Xiang-qun LI)